AGU PUBLICATIONS

JGR

Journal of Geophysical Research: Oceans

RESEARCH ARTICLE

10.1002/2017JC013350

Seasonal Cycles of Oceanic Transports in the Eastern Subpolar North Atlantic

Stefan F. Gary[1], Stuart A. Cunningham[1], Clare Johnson[1], Loïc Houpert[1], N. Penny Holliday[2], Erik Behrens[3], Arne Biastoch[4], and Claus W. Böning[4]

[1]SAMS, Scottish Marine Institute, Oban, UK, [2]National Oceanography Centre, European Way, Southampton, United Kingdom, [3]National Institute for Water and Atmospheric Research (NIWA), Wellington, New Zealand, [4]GEOMAR—Helmholtz Centre for Ocean Research Kiel, Kiel, Germany

Abstract The variability of the Atlantic Meridional Overturning Circulation (AMOC) may play a role in sea surface temperature predictions on seasonal to decadal time scales. Therefore, AMOC seasonal cycles are a potential baseline for interpreting predictions. Here we present estimates for the seasonal cycle of transports of volume, temperature, and freshwater associated with the upper limb of the AMOC in the eastern subpolar North Atlantic on the Extended Ellett Line hydrographic section between Scotland and Iceland. Due to weather, ship-based observations are primarily in summer. Recent glider observations during other seasons present an opportunity to investigate the seasonal variability in the upper layer of the AMOC. First, we document a new method to quality control and merge ship, float, and glider hydrographic observations. This method accounts for the different spatial sampling rates of the three platforms. The merged observations are used to compute seasonal cycles of volume, temperature, and freshwater transports in the Rockall Trough. These estimates are similar to the seasonal cycles in two eddy-resolving ocean models. Volume transport appears to be the primary factor modulating other Rockall Trough transports. Finally, we show that the weakest transports occur in summer, consistent with seasonal changes in the regional-scale wind stress curl. Although the seasonal cycle is weak compared to other variability in this region, the amplitude of the seasonal cycle in the Rockall Trough, roughly 0.5–1 Sv about a mean of 3.4 Sv, may account for up to 7–14% of the heat flux between Scotland and Greenland.

Key Points:
- The seasonal cycle of eastern North Atlantic volume transport has a moderate amplitude with weakest northeastward transport in summer
- The weakest transports in summer are consistent with seasonal changes in the gradient of the regional wind stress curl
- Volume transport dominates temperature and freshwater transports

Correspondence to:
S. F. Gary,
stefan.gary@sams.ac.uk

Citation:
Gary, S. F., Cunningham, S. A., Johnson, C., Houpert, L., Holliday, N. P., Behrens, E., . . . Böning, C. W. (2018). Seasonal cycles of oceanic transports in the Eastern Subpolar North Atlantic. *Journal of Geophysical Research: Oceans*, *123*, 1471–1484. https://doi.org/10.1002/2017JC013350

Received 10 AUG 2017
Accepted 23 JAN 2018
Accepted article online 1 FEB 2018
Published online 27 FEB 2018

1. Introduction

The northward flows of warmer, saltier, and shallower waters and the southward flows of colder, fresher, and deeper waters that make up the Atlantic Meridional Overturning Circulation (AMOC) play a role in the global redistribution of heat and freshwater. It is through this role that the AMOC is also likely to be a source of skill for seasonal to decadal predictions of sea surface temperatures, which, in turn, may have wide reaching impacts (Smith et al., 2014).

A substantial fraction of the net northward, warm flow that comprises the upper limb of the AMOC traverses the Eastern Subpolar North Atlantic (ESPNA) (Figure 1). Within the ESPNA, in the Rockall Trough, the seasonal to decadal variability of water properties and mixed layer depth are reasonably well established (Ellett & Jones, 1994; Holliday et al., 2000, 2015). However, the seasonal variability in the transport of water, temperature, and salt is much less clear and likely highly aliased due to infrequent sampling relative to the time scale of the mesoscale variability in this region (Holliday et al., 2000; Sherwin et al., 2015).

In the context of recent observations, the Rockall Trough is the eastern termination for the international Overturning in the Subpolar North Atlantic Program (OSNAP) (Lozier et al., 2016). OSNAP, along with its subtropical complement, RAPID, both measure the AMOC. Previous results from RAPID at 26°N suggest that the eastern boundary of a trans-basin observing system has the potential to contribute a significant amount of the seasonal variability to the overall basin-wide estimates of the AMOC (Kanzow et al., 2010). Furthermore, Kanzow et al. (2010) show that the phasing of the seasonal cycle relative to infrequent observations is an essential context for interpreting the observations. AMOC time series from the first two years of the OSNAP observations will be available soon but it is likely that longer time series will be required before a clear seasonal cycle can be obtained. Determining the seasonal cycle of the transports in the Rockall Trough will

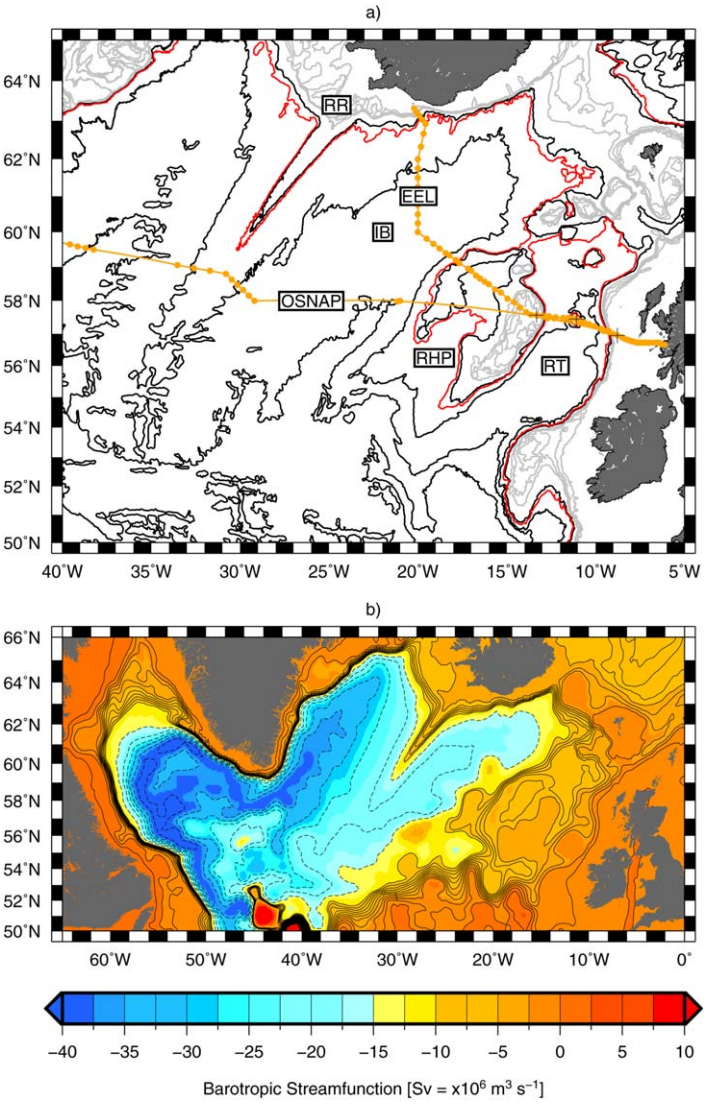

Figure 1. (a) Bathymetry of the Eastern Subpolar North Atlantic (ESPNA) contoured at 1,000 m intervals (black) and at 100 m intervals for waters shallower than 500 m (gray). RT is the Rockall Trough, RHP is the Rockall-Hatton Plateau, IB is the Iceland Basin, and RR is the Reykjanes Ridge. The hydrographic stations (moorings) are shown for the Extended Ellett Line (OSNAP) in orange. The 1,200 m isobath, the depth at which the RT is enclosed north of the EEL, is shown with a red line. Black plus signs in the RT along the EEL are the three section waypoints used for computing geostrophic transports. (b) 1958–2009 time-mean barotropic stream function from the VIKING20 model. Streamlines are shown with dashed contour lines from −40 to −10 Sv at 5 Sv intervals and with solid contour lines from −10 to 10 Sv at 1 Sv intervals. The two different sets of contour lines are shown to highlight the core of the Subpolar Gyre in the center of the basin (dashed) and the throughput on the eastern side associated with branches of the North Atlantic Current (solid), similar to other flow schematics for this region (Holliday et al., 2015) and the broader subpolar North Atlantic (Daniault et al., 2016). In both Figures 1a and 1b, small, closed contour lines are omitted for clarity.

improve our understanding of the sources of AMOC variability and this understanding has the potential for providing a context for interpreting predictions as well as OSNAP observations.

Here we use a database of hydrographic observations from 1950 to 2015, whose core is the Extended Ellett Line (EEL) repeat hydrographic section which started in 1975, to estimate the seasonal cycle of geostrophic transports above 1,200 m, the depth at which the Rockall Trough is closed to the north (Figure 1). Wintertime observations are particularly scarce due to more challenging conditions at sea so new observations made by gliders from 2009 to 2015, in addition to ships and profiling floats, will be used here. In section 2, we outline our data sources and the processing of hydrographic observations. In section 3, we present estimates for the observed seasonal cycle of geostrophic transports along with comparable values from eddy-resolving ocean models. In section 4, we discuss the results in light of the large-scale wind forcing in this region and in section 5 we present our conclusions.

2. Methods

2.1. Data Sources

2.1.1. Hydrographic Observations

All available bottle, CTD, and profiling float hydrographic data with temperature, *T*, salinity, *S*, and pressure, *P*, from 1950 to 2015 in the region from 30°W to 0°W and from 50°N to 65°N in the updated World Ocean Database (Boyer et al., 2013) were downloaded on 6 August 2015. Data quality profile flags 0–2 (accepted, failed annual standard deviation check, two or more density inversions) and observation flags 0–3 (accepted, failed broad range check, failed inversion check, failed gradient check), 5–7, and 9 (any combination of observation flags 1–3) were allowed. After removing all duplicate profiles and profiles in water shallower than 200 m, 65.4×10^3 profiles consisting of 3.3×10^6 individual (*T*, *S*, *P*) scans were incorporated into the database. Furthermore, 13.5×10^3 profiles consisting of 4.8×10^6 *T*, *S*, *P* data points from 11 glider missions for the EEL (Holliday & Cunningham, 2013), OSNAP (Lozier et al., 2016), and Fluxes Across Sloping Topography of the Northeast Atlantic (FASTNEt) (Porter et al., 2016) programs from 2009 to 2015 were added to the database. All glider data cover the upper 1,000 m, were collected in water deeper than 200 m, and were reprocessed with basestation 2.08 (UW, 2013). Only dives with at least 70% good data, as determined by the basestation, were used.

2.1.2. Sea Surface Data Sets

Wind stress and wind stress curl were computed over the ESPNA based on 10 m winds in the CORE 2 (1948–2009) (Large & Yeager, 2009) and CCMP (1987–2011) (Atlas et al., 2011) data using neutral drag coefficients specified by Large and Yeager (2009) and Smith (1980), respectively. The two wind data sets are included here to check for consistency in the wind stress curl results. The delayed-time absolute dynamic topography (ADT) of the sea surface altimeter product from 1993 to 2014 was produced by Ssalto/Duacs and distributed by Aviso, with support from Cnes (http://www.aviso.altimetry.fr/duacs/).

2.1.3. Ocean Model Output

The VIKING20 configuration (Böning et al., 2016) of the NEMO ocean general circulation model (Madec, 2008) is a 0.05° resolution model of the North Atlantic two-way nested within a 0.25° global ocean/sea-ice model (Debreu et al., 2008). The model is divided into 46 *z*-levels with spacing increasing gradually from

6 m at the surface to a maximum of 250 m at depth. The bottom cells have partial depths to better reflect bathymetry (Barnier et al., 2006). The model was started from rest with climatological *T* and *S* (Levitus et al., 1998). CORE 2 atmospheric data and bulk formulae (Large & Yeager, 2009) were used force the model with an initial spin-up of only the 0.25° base model from 1978 to 2007 followed by a fully nested hindcast from 1948 to 2009. VIKING20 has been compared to observations from intraseasonal (Fischer et al., 2015) to interannual (Breckenfelder et al., 2017; Mertens et al., 2014) time scales.

To check for consistency of results in a different eddy-resolving model, output from the regional FLAME 0.08° configuration of MOM2.1 (Böning et al., 2006; Pacanowski, 1996) was used. FLAME has a similar vertical discretization as VIKING20, 10–250 m spacing on 45 *z*-levels, but with full thickness bottom cells. Wind stress and heat fluxes were used to force FLAME via bulk formulas but sea surface salinity relaxation was used instead of freshwater fluxes. FLAME was initialized at rest with January anomalies (Levitus & Boyer, 1994; Levitus et al., 1994) superimposed on an annual mean field (Boyer & Levitus, 1997), spun up for 10 years under ECWMF climatological conditions, and run as a hindcast from 1990 to 2004 with interannual, monthly anomalies specified by the NCEP/NCAR reanalysis (Kalnay et al., 1996) superimposed on the initial climatological forcing. The basin-scale circulation in subtropical and subpolar gyres in FLAME are consistent with observations (Biastoch et al., 2008; Böning et al., 2006; Burkholder & Lozier, 2011; Gary et al., 2011).

2.2. Quality Control and Climatologies

Since gliders and profiling floats can operate during stormy winters, they make an important contribution to the seasonal cycle in the ESPNA. However, gliders sample the ocean on dive cycles spanning roughly 5 km while hydrographic stations for ships in the open ocean can be 30 km apart. In order to remove biases in averages due to these different data densities, we isopycnally average hydrographic profiles that fall in each 0.2° × 0.2° by 1 month bin from 1950 to 2015 across the ESPNA, consistent with the first baroclinic Rossby radius of deformation in this region of about 10 km (Chelton et al., 1998). We refer to this process as "state-binning." In our database, state-binning reduces the number of profiles by about 35%.

Although state-binning is at 0.2° × 0.2° resolution, hydrographic data quality control (QC) is performed at 1° × 1° because of limited data density. As has been done previously with Hydrobase automated QC, the first QC step is to remove any raw *T*, *S*, *P* triplets outside of ±3.0 standard deviation envelopes relative to mean *T*-*P* and *S*-*P* curves and a broad pressure-based range check (Lozier et al., 1995). Typically, the next step in Hydrobase QC is to check the data in *T*-*S* space by using the statistics of the mean *T*-*S* curves to filter out any raw *T*, *S*, *P* triplets outside of ±2.3 standard deviations relative to the mean *T*-*S* curve (Lozier et al., 1995). Our new method, on the other hand, must account for the fact that there are potentially more glider data than other platforms in a given location because gliders dive and climb much more frequently in space than ships or floats make observations. Taking a simple average of the data would bias the QC envelopes toward the glider data. Therefore, we use state-binned, not raw, data to set the envelope of acceptable data in the *T*-*S* space QC filter applied to the raw data. Any raw *T*, *S*, *P* triplets outside of ±2.3 standard deviations relative to the state-binned mean *T*-*S* curves are removed. In both the *P*-level and *T*-*S* filters, any profiles with more than 20% rejected data points are entirely rejected. Aside from the addition of state-binning to set the envelope of acceptable data and changes in resolution, the QC here is nearly identical to that described by Lozier et al. (1995) with the same Hydrobase functions (Curry & Nobre, 2013).

After two passes of the QC filter, 88.2% of the profiles and 91.8% of the *T*, *S*, *P* triplets are retained. For the glider data, 93.5% of the triplets are retained. The joint QC of ship, float, and glider data has the benefit of including all possible observed variability; if glider data were QC'ed relative to the envelope defined by just ship and float data, up to 30% of the glider data points are rejected.

Once the QC is done, the retained raw data are state-binned one last time and the resulting hydrographic profiles are sorted into four seasons (DJF, MAM, JJA, and SON), isopycnally averaged, and interpolated onto a list of standard depths to construct seasonal, three-dimensional, 0.2° × 0.2° by 10 m resolution climatologies of temperature and salinity over the ESPNA. State-binning is required here because we do not want the different spatial sampling scales in the raw, QC'ed data due to the different platforms to bias the climatologies. The seasons, DJF, MAM, JJA, and SON, are based on 7.0×10^3, 13.7×10^3, 15.3×10^3, and 9.2×10^3 state-binned profiles, respectively. Along the EEL in the Rockall Trough (14°W–8.5°W ×56.5°N–58.0°N), there are 411, 1,034, 522, and 424 state-binned profiles for DJF, MAM, JJA, and SON, respectively. Empty grid nodes are filled with linear interpolation in the vertical and along-isopycnal Laplacian-spline interpolation in

the horizontal (Smith & Wessel, 1990). To reduce the impact of mesoscale variability, each climatology is smoothed along isopycnals with a 1 grid node radius Gaussian filter with a 15 km length scale. *T* and *S* in the Rockall Trough along the EEL were extracted from each climatology and linearly interpolated onto a 5 km by 10 dbar regular grid.

All of the seasonal cycles computed in this manuscript, for both observations and models, were computed by sorting data into either four seasons or 12 months and then averaging the data in the 4 or 12 bins. In particular, the annual mean for each year was not subtracted from the data before the seasonal cycle was computed because there are insufficient observations to define the annual mean for each year. Annual means were not subtracted from the model output as well because we wanted the results based on model output to be directly comparable to the observations.

2.3. Geostrophic Transports

The sections of the Rockall Trough extracted from the seasonal, three-dimensional climatologies as described at the end of section 2.2 are used to compute geostrophic transports as described by Holliday et al. (2015) and as implemented by Morgan and Pender (2010) except that bottom triangles are treated with zero transport and the geostrophic transport is referenced to a level of no motion at 1,200 dbar (Holliday et al., 2000) instead of an isopycnal. All transports presented here are over the upper 1,200 m. Due to the relatively high spatial resolution of the climatologies, the contribution of bottom triangles to the net transports above 1,200 dbar are negligible. Therefore, geostrophic transports discussed here, designated as V_{geo}^{1200}, represent the upper 1,200 m and are all relative to 1,200 dbar. V_{geo}^{1200} in observations and models are computed the same way. For comparison with model output, it is also useful to define the absolute transport over the upper 1,200 m, V_{abs}^{1200}, which is the direct integration of the model absolute, not relative, velocity field over the upper 1,200 m across the Rockall Trough. V_{abs}^{1200} is only available from model output and is not estimated from observations.

Since seasonal changes in the barotropic flow could impact the level of no motion and isopycnals, rather than isobars, are also used to reference geostrophic flow in other studies, sensitivity tests with levels of no motion over a range of isopycnals were carried out. There were no significant impacts on the seasonal cycle of transports in the Rockall Trough for isopycnals from σ_θ=27.60 to σ_θ=27.80 kg m^{-3}. Furthermore, previous work has shown that the optimum isopycnal reference level for the Rockall Trough, σ_θ=27.68 kg m^{-3}, is constrained to a narrow range of ±0.02 kg m^{-3} with an estimate for the error due to a time-invariant reference level at ±0.2 Sv (Holliday et al., 2015). Finally, it will be shown below that, in the Rockall Trough, there is good agreement between V_{geo}^{1200} and V_{abs}^{1200} in the output of the two eddy-resolving models presented in this study.

Temperature and freshwater transports are relative to 0°C (Bacon & Fofonoff, 1996) and 34.8 PSU (Serreze et al., 2006), respectively. The temperature transport is computed by integrating the product of the northward geostrophic or absolute velocities, v_{geo}^{1200} or v_{abs}^{1200}, respectively, with the in situ density, ρ, surface-referenced heat capacity, C_P, and surface-referenced potential temperature, θ, over the area of the Rockall Trough section,

$$\text{temperature transport} = \int v \rho C_P \theta \, dA, \tag{1}$$

as in Bacon and Fofonoff (1996). The freshwater transport is computed by

$$\text{freshwater transport} = \int v \frac{(S_{ref} - S)}{S_{ref}} \, dA \tag{2}$$

where S is the salinity and S_{ref}=34.8 is the reference salinity.

2.4. Geostrophic Stream Function

A geostrophic transport stream function, ψ, is estimated by first computing the dynamic height referenced to 1,200 dbar, then depth-integrating the dynamic height from 1,200 to 10 m, and finally dividing by the local Coriolis parameter

$$\Psi = \frac{1}{f}\int_{z_{deep}}^{z_{surf}}\int_{P_{ref}}^{P_{surf}} \delta dPdz \tag{3}$$

where P_{ref} is the reference pressure (1,200 dbar), z_{deep} is the deepest level of the upward integration (1,200 m), P_{surf} and z_{surf} are the surface values, δ is the specific volume anomaly, and f is the local Coriolis parameter. Here Ψ is computed from the T, S, P data after the data have been quality-controlled and state-binned. Once Ψ is computed at the 0.2° × 0.2° by 1 month resolution of the state-binned data, all points in the same spatial bins for each season are averaged to create time-mean, seasonal maps. Bins with less than 10 profiles are selectively smoothed with a 5 grid point radius filter whose weighting depends on the number of profiles and separation from the central bin as in Lozier et al. (1995). Seasonal Ψ anomalies were computed by taking the difference between the Ψ maps for a particular season and the average Ψ map over all four seasons.

2.5. Sverdrup and Ekman Transports

The wind-driven Sverdrup (Sverdrup, 1947) and Ekman transports were computed as summarized in Gray and Riser (2014);

$$V_{geo} = V_{Sv} - V_{Ek} = \left(\frac{1}{\rho\beta}\boldsymbol{k}\cdot\nabla\times\boldsymbol{\tau}\right) - \left(\frac{-\tau_x}{\rho f}\right), \tag{4}$$

where V_{Sv} and V_{Ek} are the Sverdrup and Ekman transports, respectively, β is the meridional gradient of f, $\boldsymbol{k}$ is the vertical unit vector, $\boldsymbol{\tau}$ is the vector wind stress, and τ_x is the zonal component of the wind stress. The vertical velocity at the base of the Ekman layer, Ekman pumping, was computed with

$$w_{Ek} = \boldsymbol{k}\cdot\nabla\times\frac{\boldsymbol{\tau}}{\rho f}. \tag{5}$$

Ekman transports were not included in our analysis because integrated over a zonal line spanning the Rockall Trough, Ekman transports are at least an order of magnitude smaller than the Sverdrup transports and volume transports in the annual mean and seasonally. The time-mean Sverdrup and Ekman transports over the Rockall Trough based on monthly time series from the CORE 2 data are 1.4 ±3.4 and −0.1±0.2 Sv, respectively.

3. Results

3.1. Seasonality of Absolute Dynamic Topography

An estimate of the seasonality of transport in the broader ESPNA region is provided by seasonal anomalies of ADT of the sea surface (Figure 2). The seasonal anomalies are computed by taking the difference between the average of all ADT fields for a particular season and the average over all ADT fields. Despite averaging over more than two decades, mesoscale variability is still present, especially at the energetic Subpolar-Subtropical Gyre boundary south of about 54°N. Seasonal anomalies are dominated by thermal expansion and contraction with the coldest waters in the spring, after the winter storms (Figure 2b), and the warmest waters in the fall, lagging the summer warming (Figure 2d).

In the time-mean (Figure 2e), as defined by a closed contour of ADT (Foukal & Lozier, 2016), the core of the Subpolar Gyre is west of about 30°W. East of 30°W, a positive zonal gradient in ADT is consistent with the northeastward North Atlantic Current. Between about 34°W–22°W × 55°N–60°N, an anomalous ADT low in winter transitions to a high in summer (Figures 2a and 2c). At the same time, along the eastern boundary, a high ADT anomaly in winter becomes a low in the summer. The result is a seasonal change in sign of the zonal gradient in ADT anomaly from about 55°N to 60°N. Consistent with the large-scale maps, Figure 2f shows both the seasonal rise and fall of ADT due to thermal expansion as well as highlights the seasonal change in the zonal gradient of ADT anomalies along 58°N. As noted above, in DJF (JJA), the basin-wide slope of ADT is positive (negative) suggesting northward (southward) anomalous flow in winter (summer). However, the strong temporal variability relative to the seasonal cycle must be acknowledged; while the standard error in each seasonal mean of Figure 2f is on the order of the thickness of the lines, the standard deviation, which represents the mesoscale to interannual variability, is on the order of the width of the plot (not shown). This variability presents a challenge to using ADT to infer changes in transport.

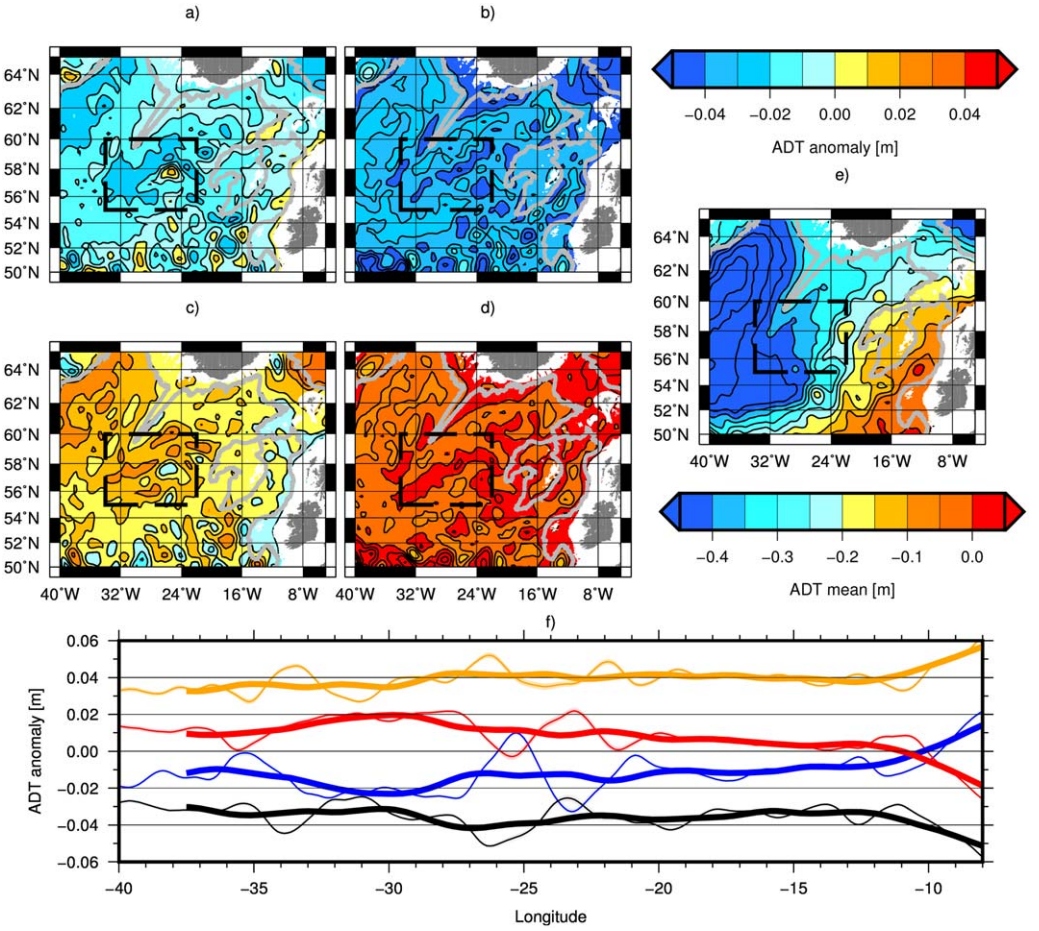

Figure 2. Seasonal anomalies of Absolute Dynamic Topography (ADT) of the sea surface for (a) DJF, (b) MAM, (c) JJA, and (d) SON relative to (e) the 1993–2014 mean. Gray lines are the 1,200 m isobath and shading is clipped to the 200 m isobath. The dashed black box marks the region from 34°W to 22°W by 55°N to 60°N referred to in the text. (f) Seasonal ADT anomalies along 58°N for DJF (blue), MAM (black), JJA (red), and SON (orange). The thin lines are ADT at the original 0.25° resolution of the data and the thick lines are smoothed with a 5° wide boxcar filter. Contours of ADT reflect pressure gradients on the water column due to the sea surface so they are geostrophic streamlines near the surface.

3.2. Seasonality of Geostrophic Stream Function

Next, we test for seasonality in pressure gradients at depth over the whole ESPNA. Geostrophic stream Functions, Ψ, representing the upper 1,200 m are constructed from our database of state-binned hydrographic data (Figures 3a–3d). In general, these stream functions exhibit northeastward flow (Figures 3e–3h). Packed contours in the southwest opening to the northeast reflect the branching of the North Atlantic Current between the Rockall Trough and the rest of the basin, similar to the barotropic stream function in the VIKING20 model (Figure 1b) and basin-scale observational synthesis (Daniault et al., 2016).

The seasonal anomalies of geostrophic stream function (Figures 3i–3l) broadly match the seasonal heating and cooling as reflected in ADT anomalies (Figures 2a, 2b, 2c, 2d, and 2f) with generally lower values in MAM and higher values in SON distributed over the ESPNA. Furthermore, the seasonal reversal of the zonal gradient of ADT anomalies noted above is also present in geostrophic stream function anomalies. A low in the Iceland Basin in DJF, centered at 58°N, 23°W, (Figures 2a, 2f, and 3i) transitions to a high in JJA (Figures 2c, 2f, and 3k) and vice versa near the eastern boundary. Seasonal anomalies of dynamic height (not shown) follow nearly identical patterns as the geostrophic stream function anomalies (Figures 3i–3l) which is consistent with the fact that the geostrophic stream function presented here is a vertical integral of the dynamic height. The same spatial patterns in the seasonal anomalies of geostrophic stream function in the Iceland Basin, and to a much weaker extent at the eastern boundary, emerge when using a range of isopycnals from σ_θ=27.40 to σ_θ=27.80 kg m^{-3} as reference levels (not shown).

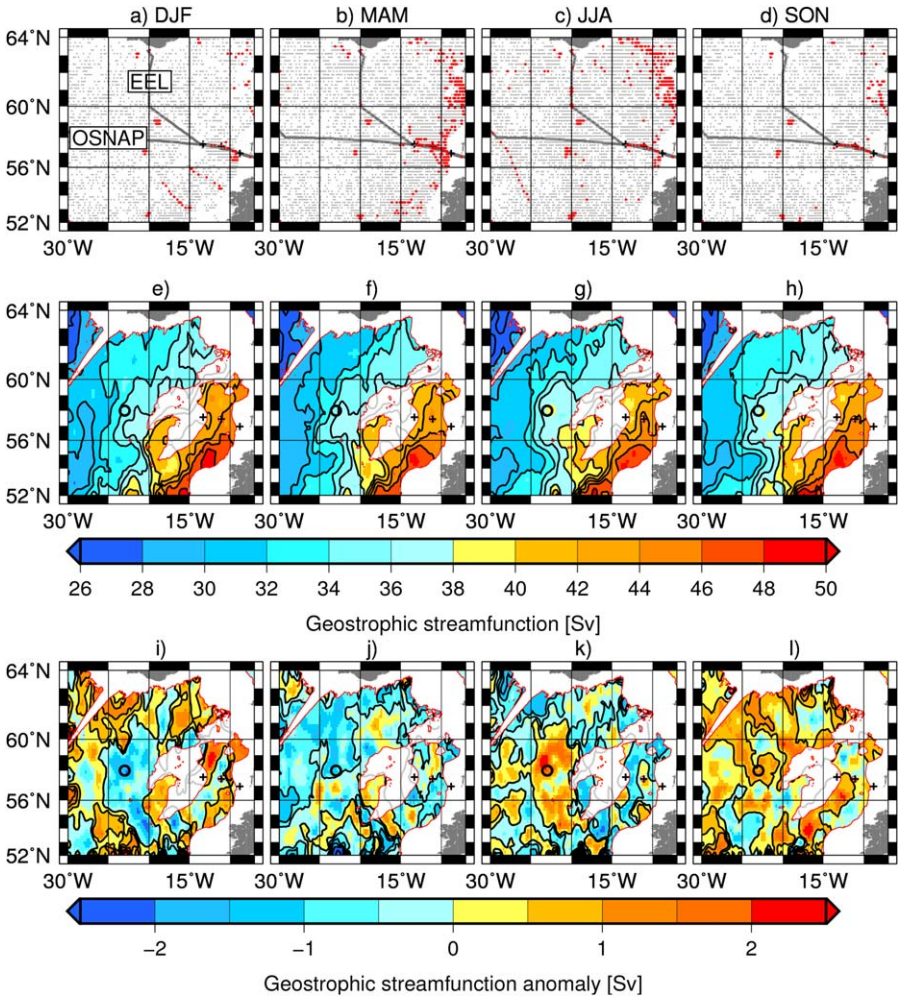

Figure 3. More than 5 QC'ed, state-binned hydrographic profiles in each 0.2° × 0.2° bin are shown with red dots for (a) DJF, (b) MAM, (c) JJA, and (d) SON. Gray dots are bins with 5 or fewer profiles. The mean geostrophic stream function, Ψ, for each season is contoured at 2 Sv intervals (black lines) for (e) DJF, (f) MAM, (g) JJA, and (h) SON. The Ψ anomaly corresponding to each season is shown in (i) through (l) with 0.5 Sv contour intervals (black lines). The red line is the 1,200 m isobath. Gray lines in regions shallower than 1,200 m are spatially interpolated, not calculated, contours. In Figures 3e–3l, closed contour lines, which represent local recirculation, are omitted for clarity. The Rockall Trough section waypoints are marked by +'s while 58°N, 23°W, a point referred to in the text, is marked with a bold circle.

Despite averaging over decades of observations, noise due to the aliasing of mesoscale eddies by the observations is still evident with significant local curvature in the streamlines (Figures 3e–3l). Although there is a seasonal change in the center of the Iceland Basin, suggesting a seasonal spin-up and spin-down of a local recirculation, the seasonal anomalies of the net flow through the region are only on the order of 0.5 Sv (i.e., a net crossing of 1 contour line along a zonal line, Figures 3i–3l) and this residual flow is contorted and hard to pick out relative to the background flow of roughly 10 Sv (Figures 3e–3h). This net seasonal flow is on the order of uncertainty estimates; Holliday et al. (2015) estimate ±0.5 and ±0.2 Sv uncertainties in the Iceland Basin and Rockall Trough, respectively, when using a time-invariant reference level. Furthermore, maps of seasonal pressure anomalies on isopycnals constructed from our climatology (not shown) exhibit mesoscale variability but basin-scale, seasonal patterns of isopycnal heave are tenuous at best.

3.3. Geostrophic Transport Through the Rockall Trough Section on the EEL

Since sparse sampling has the potential to alias the large-scale patterns in Ψ presented above, we focus on one of the most data-rich regions in the ESPNA: the Rockall Trough portion of the EEL (Figures 3a–3d). Most of the winter profiles near the EEL were observed with gliders, highlighting the importance of this

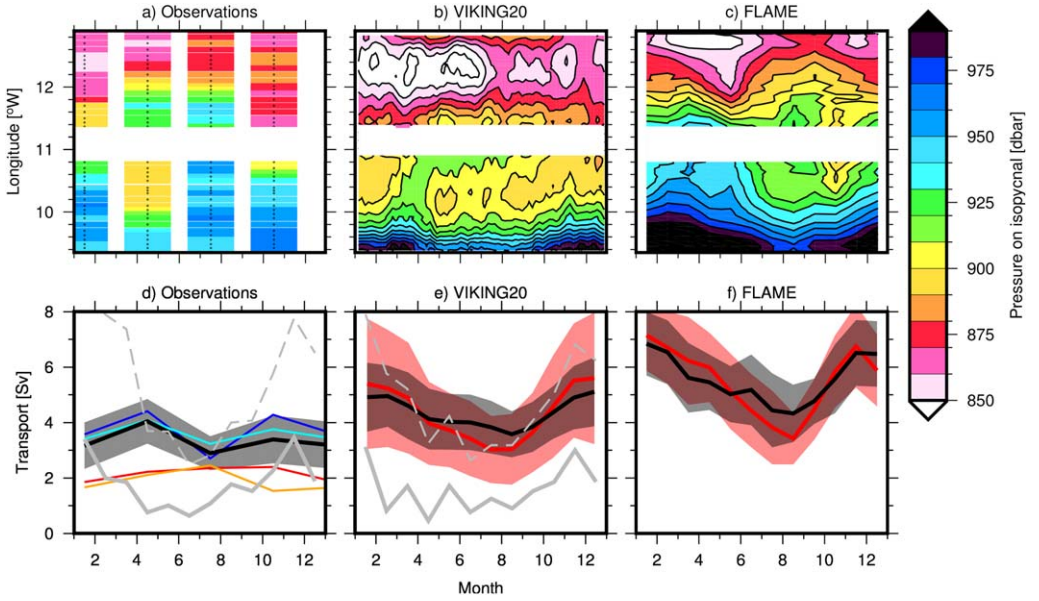

Figure 4. (a–c) Pressure on the observed σ_θ=27.50 kg m^{-3}, VIKING20 σ_θ=27.58 kg m^{-3}, and FLAME σ_θ=27.50 kg m^{-3} isopycnals along the Rockall Trough portion of the EEL. Model isopycnals were chosen to match the depth of (a). Dots in Figure 4a are climatology data points in time and space. The white band centered at 11°W is the Anton Dohrn Seamount poking up through the isopycnal surface. (d–f) Rockall Trough seasonal V_{geo}^{1200} (black lines with gray envelope), Sverdrup (gray lines with thin, dashed gray lines as envelope) and V_{abs}^{1200} (red lines with pink envelope) transports. Blue, cyan, red, and orange lines in Figure 4d are V_{geo}^{1200} computed from observational climatologies at 0.15°, 0.25°, 0.5°, and 1.0° resolutions, respectively, to show the sensitivity of the black line (0.2° climatology) to resolution. Envelopes for models and Sverdrup transports are ±1 standard deviation computed from monthly values. Sverdrup transports were computed from (d) CORE2 and (e) CCMP. Sverdrup transports from FLAME are not shown in Figure 4f because the 15 years of FLAME output are not sufficiently long to filter out the interannual variability in the wind stress curl so the results are too noisy to be meaningful here.

observational platform. Since the glider missions span 2009–2015, the winter data are strongly weighted toward this time period. On the EEL, the seasonal heave of a middepth isopycnal (Figure 4a) shows that the zonal gradient of pressure on an isopycnal is weakest in the summer, consistent with two eddy-resolving models (Figures 4b and 4c). The observed isopycnal is located at the interface between the permanent thermocline and the upper waters (Holliday et al., 2015). It was chosen because it lies within the 1,000 m maximum operating depth of gliders but below the maximum depth of the winter mixed layer of about 800 m (Holliday et al., 2000). Similar patterns are visible on deeper isopycnals in the models but not in observations because there are insufficient winter and fall observations below 1,000 m so the effects of interpolation and smoothing dominate the climatologies and unrealistically flatten isopycnals.

The vertical shear of geostrophic velocity is proportional to the tilt of isopycnals so, integrating from 1,200 m to the surface, the weakest V_{geo}^{1200}, in summer, coincides with periods when the isopycnals are flattest in models and observations (Figure 4). However, even with full knowledge of *T*, *S* and velocity in the models, the mesoscale and interannual variability in V_{geo}^{1200} and V_{abs}^{1200}, as shown by the gray and pink envelopes, is on the order of the amplitude of the seasonal cycle (Figures 4e and 4f).

3.4. Uncertainty Estimates for Observed Geostrophic Transport

While the uncertainty in the seasonal cycle of transport can be explicitly computed for model output, estimates for the uncertainty of the observed transports in the Rockall Trough due to both observational aliasing and any bad data that survived the QC process are made with a bootstrapping process. One Hundred seasonal climatologies are constructed using random subsets of the raw hydrographic database. The uncertainty is estimated as 1 standard deviation of the geostrophic transport in the random-subset climatologies. The uncertainties increase with the percentage of data removed (Figure 5). An inflection point near 50% of data removed represents a balance between causing the climatology building process to break down by removing too much data and repeatedly building nearly the same climatology when too little data is

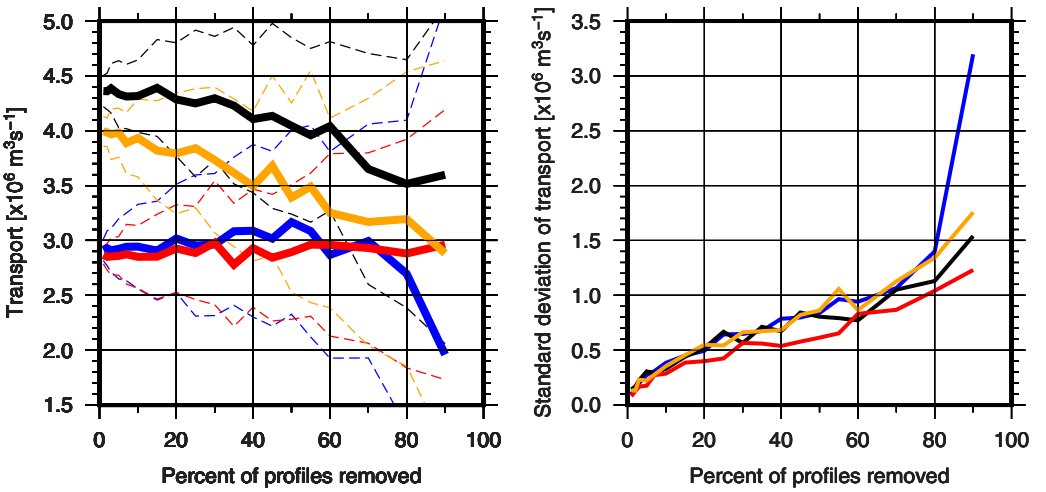

Figure 5. Sensitivity of volume transport, and its uncertainty, to the fraction of the data randomly removed from the climatology building process for each season. (a) Mean (solid) and ±1 standard deviation envelope (dashed) and (b) standard deviation only of V_{geo}^{1200} on the Rockall Trough portion of the Extended Ellett Line computed from 100 climatologies constructed with different amounts of data removed. Each line corresponds to a different season: blue for DJF, black for MAM, red for JJA, and orange for SON. The standard deviations in Figure 5a are shown alone in Figure 5b to highlight the inflection point in the variability at about 50% data removed.

removed. Therefore, we chose the 50% random removal level for the mean and uncertainty of the transports we report here. Since these uncertainties do not take into account all the variability in the real ocean, they should be interpreted as analogous to standard errors in the mean transport and not the standard deviation of the transport. Similar to the model output, the uncertainty estimate of the observed volume transports (Figure 4d) is also on the order of the seasonal cycle amplitude.

The Rockall Trough volume transports derived from observations can be sensitive to the horizontal resolution of the grid used to average over the data. For horizontal grids in the range of 0.15–0.25° (Figure 4d blue, black, and cyan lines), there is no significant change in the transports relative to the envelope of uncertainty. However, the isopycnals in coarser, lower resolution climatologies are much flatter than in the higher resolution climatologies (not shown), resulting in smaller pressure gradients at depth and thus reduced transports at low resolution (Figure 4d, red and orange lines). We focus on results based on the

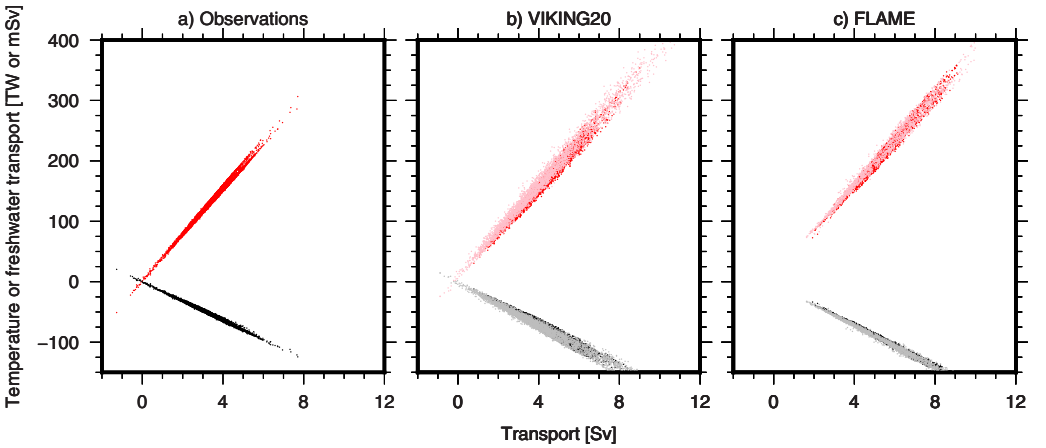

Figure 6. Volume transport versus temperature (red and pink) and freshwater (black and gray) transports in the Rockall Trough for (a) observations, (b) VIKING20, and (c) FLAME. V_{geo}^{1200} data points are shown by black and red dots while V_{abs}^{1200} data are in gray and pink. In Figure 6a, all the transports from all the climatologies constructed by bootstrapping (Figure 5) are plotted here. In Figures 6b and 6c, transports from each available model field are shown at 5 day mean and 3 day snapshot intervals, respectively.

Table 1
Correlations and Slopes Between Volume Transport and Other Transports in the Rockall Trough

	Volume versus R^2	Temperature (TW Sv^{-1})	Volume versus R^2	Salt (10^6 kg s^{-1} Sv^{-1})	Volume versus R^2	Freshwater (mSv Sv^{-1})
Observations	0.99	37.9	0.99	36.4	0.99	−16.2
VIKING20-Geo.	0.98	37.1	0.99	36.4	0.95	−17.6
VIKING20-Abs.	0.99	37.1	0.99	36.5	0.98	−17.6
FLAME-Geo.	0.98	37.8	0.99	36.5	0.99	−17.6
FLAME-Abs.	0.99	37.0	0.99	36.4	0.99	−17.1

Note. Geo. and Abs. are computed with the geostrophic and absolute velocity fields, respectively.

observations gridded at 0.2° resolution because 0.2° is the resolution of the state-binning, is on the order of the baroclinic Rossby radius of deformation in this region, and lies within the range of relative insensitivity of transport to resolution.

3.5. Relating Volume, Temperature, Salt, and Freshwater Transports

Once Rockall Trough volume transports are quantified, the next step is to estimate temperature, salt, and freshwater transports. Rockall Trough volume transports in observations and models dominate the variability of the associated temperature, salt, and freshwater transports. At least 95% of the variability in the other transports is explained by the volume transport (Figure 6 and Table 1). In the models, regression slopes

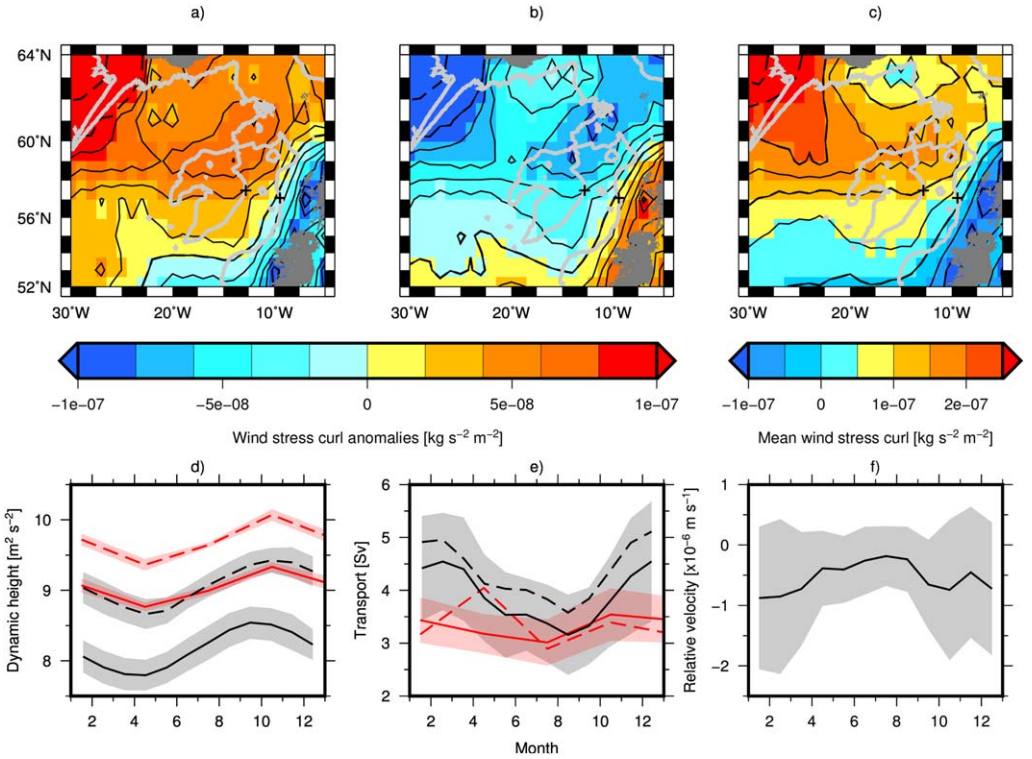

Figure 7. Seasonal wind stress curl anomalies for (a) DJF and (b) JJA with (c) the time-mean wind stress curl from 1948 to 2009 CORE2 data (Large & Yeager, 2009). Black + symbols on the 1,200 m isobath are the endpoints of the section. Seasonal anomalies in CCMP data (Atlas et al., 2011) are similar. Solid contour lines are at 2×10^{-8} kg s^{-2} m^{-2} and 5×10^{-8} kg s^{-2} m^{-2} for anomalies and the mean, respectively. Dashed contour lines are at 1×10^{-7} kg s^{-2} m^{-2} intervals. (d) Seasonal dynamic height, relative to 1,200 dbar, at the Rockall Trough EEL section endpoints near the 1,200 m isobath at 12.79°W (solid) and 9.43°W (dashed) in observations (red) and VIKING20 (black). (e) Geostrophic transport derived from the difference in depth-integrated dynamic heights at the endpoints in observations (red) and VIKING20 (black). The red dashed line is the observed V_{geo}^{1200} (the black line in Figure 4d) and the black dashed line is V_{geo}^{1200} in VIKING20 (the black line in Figure 4e). (f) Mean Ekman pumping velocities at 9.43°W relative to 12.79°W derived from the CORE2 data.

between volume transport and associated transports are nearly identical for transports computed with geostrophic velocities or absolute velocities. The regression slopes for the observational estimates of the transports, 37.9 TW Sv^{-1}, 36.4×10^6 kg s^{-1} Sv^{-1}, and -16.2 mSv Sv^{-1} for temperature, salt, and freshwater transports, respectively, are comparable to the model-derived slopes.

3.6. Using Rockall Trough Section Endpoints to Estimate Geostrophic Transport

A second framework for assessing the upper layer volume transports in the Rockall Trough is based on the section endpoints. The transports presented above required the use of *T* and *S* from across the whole section; using endpoints alone to estimate volume transports may filter out some of the aliasing due to eddies in the center of Rockall Trough. The disadvantage to this approach is that it can be used only in waters with at least the same common depth, in this case the reference level of 1,200 m, so wedges on the sides of Rockall Trough with waters shallower than 1,200 m are neglected.

There is a clear seasonal cycle in dynamic height near the 1,200 m isobath at the eastern and western endpoints of the Rockall Trough (Figure 7d). The resulting transport estimates for the waters above 1,200 m are consistent with summer having the lowest volume transport. Furthermore, seasonal anomalies of wind stress curl in the eastern subpolar North Atlantic show a reversal of the gradient in the wind stress curl anomaly across the Rockall Trough from winter to summer (Figures 7a and 7b), which results in a seasonal change in the relative Ekman pumping, $w_{east}-w_{west}$, at the eastern and western edges of the Rockall Trough (Figure 7f). The weakest difference in the local Ekman pumping at the endpoints coincides with the weakest transport in the Rockall Trough (Figures 7e and 7f).

4. Discussion

4.1. Seasonality of Wind Stress Curl as the Driver for Rockall Trough Transports

Over long time scales, Sverdrup dynamics predict that the wind-driven transport will match the geostrophic transport in the upper layer (Gray & Riser, 2014; Sverdrup, 1947). However, on shorter, seasonal time scales, the Sverdrup transport (i.e., the wind stress curl) drives a primarily barotropic response (Kanzow et al., 2010, and references therein). Kanzow et al. (2010) show that the seasonal baroclinic response is associated with spatial gradients in wind stress curl, and not necessarily with the wind stress curl itself. Wind stress curl anomalies drive local anomalous Ekman sucking (+curl) or anomalous Ekman pumping (−curl), which, in turn, locally heave the isopycnals relative to each other, impact horizontal gradients of dynamic height, and change geostrophic transport. In summary, local wind stress curl is related to local dynamic height so the baroclinic transport, which is dependent on gradients of dynamic height, also depends on gradients in wind stress curl. However, this simplified framework does not account for local perturbations moving as waves or interacting with topography.

Support of this proposed mechanism can be found in the transport calculated from the endpoints of the Rockall Trough section. When the magnitude of the seasonal wind stress curl gradient, quantified by the relative Ekman velocity between the two endpoints, is weak (strong), the gradient in the dynamic heights at the endpoints, which is directly related to the transport through the Trough, is also weak (strong) (Figures 7e and 7f). The direct impact of this Ekman pumping mechanism is estimated by vertically shifting the time-mean *T* and *S* profiles at the Rockall Trough endpoints relative to each other by 15 m. The shift is based on the magnitude of the relative Ekman pumping velocities in Figure 7f: about 1×10^{-6} m s^{-1} over 6 months. Geostrophic transport with and without the shift is computed. The resulting change in transport due to the shift is about 0.5 and 0.4 Sv in observations and VIKING20, respectively. While 0.5 Sv is on the order of the amplitude of the observed transport seasonal cycle, it is less than half of the signal in VIKING20. Although there is considerable variability in the relative Ekman velocities, the shift of 15 m used here may be an overestimate since there is likely a seasonal ramping up and down of the relative Ekman velocities rather than a constant value; smaller shifts result in yet smaller amplitudes of the transport seasonal cycle.

The amplitude of the seasonal cycle of V_{geo}^{1200} in the models, 1.5 and 2.5 Sv for VIKING20 and FLAME, respectively, is less than that for V_{abs}^{1200}, 2.6 and 3.7 Sv for VIKING20 and FLAME, respectively (Figures 4e and 4f). Although small compared to the interannual variability, this seasonal discrepancy between geostrophic and absolute transports may stem from the wind-driven circulation imparting a seasonal barotropic transport that is not in the geostrophic velocity field. This seasonal modulation is consistent with the seasonal

intensity of the Sverdrup transport (Figures 4d and 4e) because when the Sverdrup transport is low, $V_{abs}^{1200} < V_{geo}^{1200}$ but when the Sverdrup transport is high, $V_{abs}^{1200} > V_{geo}^{1200}$. Insofar as the gradient of seasonal ADT anomalies (Figure 2) can be an indicator of the seasonal barotropic transport, the lower (higher) transport in the summer (winter) is also consistent with this modulation.

4.2. Comparing Observations to Previous Work and Model Output

The geostrophic transports presented here are consistent with previous estimates of 3.7 ±2.4 and 2.3 ±1.3 Sv (Holliday et al., 2000, 2015). The phasing and magnitude of the seasonal transports presented here are also broadly consistent with estimates downstream of the Rockall Trough in the Faroe-Shetland Channel (Berx et al., 2013). Upstream of the Rockall Trough, there is evidence for weaker trans-basin transports in the late spring and summer between Portugal and Greenland (Mercier et al., 2015).

The observed transport estimates presented here are lower compared to the model transports (Figures 4d, 4e, 4f, and 7e), possibly due to the along-isopycnal smoothing applied to climatologies to filter out some of the mesoscale variability. Smoothing results in weaker gradients and reduces V_{geo}^{1200} (e.g., Figure 4d). In contrast, the model output was not spatially smoothed. Observations made by OSNAP moorings in the Rockall Trough will eliminate the need for spatial smoothing so they will likely estimate higher volume transports than the transports presented here. The high mesoscale to interannual variability means that continuous boundary monitoring, as is implemented by OSNAP, is a good approach for an observing system in the Rockall Trough.

In both models and observations, the amplitude of the seasonal cycle of transports is on the order of the other variability and sources of error (Figures 4 and 7). In the models and reanalysis fields, the ±1 standard deviation envelopes that we present offer an estimate of the combined mesoscale and interannual variability because they quantify the scatter of what remains after taking monthly averages. Partitioning this variability into temporal bands is beyond the scope of this work as our goal is to show the seasonal cycle in the context of all the remaining variability. For the case of the observations, the uncertainty estimates are also impacted by the effects of aliasing and any spurious data points that did not get removed by the automated quality control process.

4.3. Rockall Trough Transports in the Context of the ESPNA Region

Finally, we situate upper 1,200 m Rockall Trough transport in the basin-scale context. Our temperature transports referenced to 0°C are an estimate of the Rockall Trough contribution to the ESPNA heat flux relative to the waters overflowing the Greenland-Scotland Ridge (initially about 0°C; Hansen & Østerhus, 2000; Jochumsen et al., 2012). The mean Rockall Trough temperature transport of 3.4 Sv × 37.9 TW Sv^{-1} = 130 TW is 46% of the 280 TW total heat flux estimate between Scotland and Greenland (Bacon, 1997). The amplitude of the Rockall Trough seasonal cycle, on the order of 0.5–1.0 Sv, translates into about 7–14% of the total Scotland to Greenland heat flux. More recently, Mercier et al. (2015) estimate that the total heat flux between Portugal and Greenland ranges between 290 and 700 TW due to strong variability of the circulation on monthly to decadal time scales. Not accounting for the fact that there are substantial changes in the water mass structure between Portugal and Scotland, a lower bound on the contribution of the time-mean Rockall Trough temperature transport to the basin-scale heat flux is potentially 19% with the seasonal cycle in the Rockall Trough accounting for another ±3%.

Similarly for salt and freshwater transports, the mean Rockall Trough salt transport of 3.4 Sv × 36.4×10^6 kg s^{-1} Sv^{-1} = 120×10^6 kg s^{-1} is up to 40% of the 303×10^6 kg s^{-1} estimate of the total northward salt transport between Greenland and Shetland (Østerhus et al., 2005) and the mean Rockall Trough freshwater transport of 3.4 Sv × 16.2 mSv Sv^{-1} = 55 mSv is up to 31% of the combined sea ice and oceanic freshwater fluxes through Fram Strait and the Barents Sea (5,800 km^3 yr^{-1} = 180 mSv) (Serreze et al., 2006). The roughly 0.5–1.0 Sv amplitude of the seasonal cycle of volume transports in the Rockall Trough is 6–12% of the mean Greenland to Shetland salt flux and 5–9% of the mean freshwater export from the Arctic to the Atlantic. All of the numbers presented here are estimates for the upper bound of the contribution of Rockall Trough transport since we do not account for recirculations between the Rockall Trough and the Greenland-Scotland Ridge or the Arctic Ocean.

5. Conclusions

We conclude that the northeastward, geostrophic transports of volume, temperature, and freshwater in the Rockall Trough are weakest in summer. Although this seasonal cycle is partly obscured by mesoscale eddies,

interannual variability, and observational aliasing, the phasing of the seasonal cycle is broadly consistent among independent observations and models, namely: hydrographic observations spanning 1950–2015; two decades of satellite altimetry; two eddy-resolving ocean circulation models; and more than six decades of reanalysis wind stress curl bias corrected by observations. In both models and observations, temperature, salt, and freshwater transports in the Rockall Trough are closely related to volume transport. Although we explicitly compute transports only in the Rockall Trough, the large-scale seasonal reversals of the gradients in the wind stress curl, sea surface height, and geostrophic stream function across the eastern subpolar North Atlantic suggest that this seasonal cycle may apply over most of the net throughput of warm waters from the Subpolar Gyre into the Nordic Seas. Finally, the transports in the Rockall Trough make, a significant contribution to the basin-scale fluxes in the subpolar North Atlantic.

Acknowledgments

We are grateful for the efforts of glider pilots: Toby Sherwin, Estelle Dumont, Mark Inall, Marie Porter, Karen Wilson, Colin Griffiths, John Beaton; and assistance recovering gliders from Brian King, Bogi Hansen, and the officers and crew of the RRS James Clark Ross, FRV Magnus Heinason, and NLB Pole Star. We are also thankful for the comments of two anonymous reviewers. The research leading to these results received funding from NACLIM, a project of the European Union 7th Framework Programme (FP7 2007–2103) under grant agreement 308299. Extended Ellett Line cruises, gliders, SFG, SAC, and NPH are supported by the NERC National Capability funding (R8-H12-85). SAC, LH, and NPH are supported by the OSNAP NERC Large grant (NE/K010700/1 and NE/K010875/1). FASTNEt gliders were supported by NERC Consortium grant NE/IO39224/1. BODC (www.bodc.ac.uk) curate the glider data. Please see text and references for other data sources. The authors will curate the observational and model data for at least 5 years after publication and it will be made available to anyone upon request.

References

Atlas, R., Hoffman, R. N., Ardizzone, J., Leidner, S. M., Jusem, J. C., Smith, D. K., et al. (2011). A cross-calibrated, multiplatform ocean surface wind velocity product for meteorological and oceanographic applications. *Bulletin of the American Meteorological Society*, *92*, 157–174. https://doi.org/10.1175/2010BAMS2946.1

Bacon, S. (1997). Circulation and fluxes in the North Atlantic between Greenland and Ireland. *Journal of Physical Oceanography*, *27*(7), 1420–1435. https://doi.org/10.1175/1520-0485(1997)027<1420:CAFITN>2.0.CO;2

Bacon, S., & Fofonoff, N. (1996). Oceanic heat flux calculation. *Journal of Atmospheric and Oceanic Technology*, *13*(6), 1327–1329. https://doi.org/10.1175/1520-0426(1996)013<1327:OHFC>2.0.CO;2

Barnier, B., Madec, G., Penduff, T., Molines, J.-M., Treguier, A.-M., Sommer, J., et al. (2006). Impact of partial steps and momentum advection schemes in a global ocean circulation model at eddy-permitting resolution. *Ocean Dynamics*, *56*(5–6), 543–567.

Berx, B., Hansen, B., Østerhus, S., Larsen, K., Sherwin, T., & Jochumsen, K. (2013). Combining in situ measurements and altimetry to estimate volume, heat and salt transport variability through the Faroe-Shetland Channel. *Ocean Science*, *9*(4), 639–654.

Biastoch, A., Böning, C. W., Getzlaff, J., Molines, J.-M., & Madec, G. (2008). Causes of interannual-decadal variability in the meridional overturning circulation of the midlatitude North Atlantic Ocean. *Journal of Climate*, *21*(24), 6599–6615. https://doi.org/10.1175/2008JCLI2404.1

Böning, C. W., Behrens, E., Biastoch, A., Getzlaff, K., & Bamber, J. L. (2016). Emerging impact of Greenland meltwater on deepwater formation in the North Atlantic Ocean. *Nature Geoscience*, *9*, 523–527. https://doi.org/10.1038/NGEO2740

Böning, C. W., Scheinert, M., Dengg, J., Biastoch, A., & Funk, A. (2006). Decadal variability of subpolar gyre transport and its reverberation in the North Atlantic overturning. *Geophysical Research Letters*, *33*, L21S01. https://doi.org/10.1029/2006GL026906

Boyer, T., Antonov, J. I., Baranova, O. K., Coleman, C., Garcia, H. E., Grodsky, A., et al. (2013). World ocean database 2013. In S. Levitus & A. Mishonov, *NOAA Atlas NESDIS* (72, pp. 1–209). Silver Spring, MD: National Oceanic and Atmospheric Administration.

Boyer, T. P., & Levitus, S. (1997). *Objective analyses of temperature and salinity for the world ocean on a 1/4 grid*. Silver Spring, MD: US Department of Commerce, National Oceanic and Atmospheric Administration, National Environmental Satellite, Data, and Information Service.

Breckenfelder, T., Rhein, M., Roessler, A., Böning, C. W., Biastoch, A., Behrens, E., et al. (2017). Flow paths and variability of the North Atlantic Current: A comparison of observations and a high-resolution model. *Journal of Geophysical Research: Oceans*, *122*, 2686–2708. https://doi.org/10.1002/2016JC012444

Burkholder, K. C., & Lozier, M. S. (2011). Subtropical to subpolar pathways in the North Atlantic: Deductions from Lagrangian trajectories. *Journal of Geophysical Research*, *116*, C07017. https://doi.org/10.1029/2010JC006697

Chelton, D. B., Deszoeke, R. A., Schlax, M. G., El Naggar, K., & Siwertz, N. (1998). Geographical variability of the first baroclinic Rossby radius of deformation. *Journal of Physical Oceanography*, *28*(3), 433–460. https://doi.org/10.1175/1520-0485(1998)028<0433:GVOTFB>2.0.CO;2

Curry, R., & Nobre, C. (2013). *Hydrobase 3* (Tech. rep.). Woods Hole, MA: Woods Hole Oceanographic Institution. Retrieved from http://www.whoi.edu/science/PO/hydrobase/php/index.php

Daniault, N., H., Mercier, P., Lherminier, A., Sarafanov, A., Falina, P., Zunino, F. F., et al. (2016). The northern North Atlantic Ocean mean circulation in the early 21st century. *Progress in Oceanography*, *146*, 142–158. https://doi.org/10.1016/j.pocean.2016.06.007

Debreu, L., Vouland, C., & Blayo, E. (2008). Agrif: Adaptive grid refinement in Fortran. *Computers & Geosciences*, *34*(1), 8–13. https://doi.org/10.1016/j.cageo.2007.01.009

Ellett, D., & Jones, S. R. (1994). *Surface temperature and salinity time-series from the Rockall Channel, 1948–1992* (36pp.). UK: Ministry of Agriculture, Fisheries and Food.

Fischer, J., J., Karstensen, R., Zantopp, M., Visbeck, A., Biastoch, E., Behrens, C. W., et al. (2015). Intra-seasonal variability of the DWBC in the western subpolar North Atlantic. *Progress in Oceanography*, *132*, 233–249. https://doi.org/10.1016/j.pocean.2014.04.002

Foukal, N. P., & Lozier, M. S. (2016). No inter-gyre pathway for sea-surface temperature anomalies in the North Atlantic. *Nature Communications*, *7*, 11333. https://doi.org/10.1038/ncomms11333

Gary, S. F., Lozier, M. S., Böning, C. W., & Biastoch, A. (2011). Deciphering the pathways for the deep limb of the meridional overturning circulation. *Deep-Sea Research, Part II*, *58*(17), 1781–1797. https://doi.org/10.1016/j.dsr2.2010.10.059

Gray, A. R., & Riser, S. C. (2014). A global analysis of Sverdrup balance using absolute geostrophic velocities from Argo. *Journal of Physical Oceanography*, *44*(4), 1213–1229. https://doi.org/10.1175/JPO-D-12-0206.1

Hansen, B., & Østerhus, S. (2000). North Atlantic-Nordic seas exchanges. *Progress in Oceanography*, *45*(2), 109–208. https://doi.org/10.1016/S0079-6611(99)00052-X

Holliday, N., Cunningham, S., Johnson, C., Gary, S., Griffiths, C., Read, J., et al. (2015). Multidecadal variability of potential temperature, salinity, and transport in the eastern subpolar North Atlantic. *Journal of Geophysical Research: Oceans*, *120*, 5945–5967. https://doi.org/10.1002/2015JC010762

Holliday, N. P., & Cunningham, S. A. (2013). The extended Ellet Line: Discoveries from 65 years of marine observations west of the UK. *Oceanography*, *26*(2), 156–163. https://doi.org/10.5670/oceanog.2013.17

Holliday, N. P., Pollard, R. T., Read, J. F., & Leach, H. (2000). Water mass properties and fluxes in the Rockall Trough, 1975–1998. *Deep-Sea Research, Part I*, *47*(7), 1303–1332.

Jochumsen, K., Quadfasel, D., Valdimarsson, H., & Jonsson, S. (2012). Variability of the Denmark Strait overflow: Moored time series from 1996–2011. *Journal of Geophysical Research*, *117*, C12003. https://doi.org/10.1029/2012JC008244

Kalnay, E., M., Kanamitsu, R., Kistler, W., Collins, D., Deaven, L., Gandin, M., et al. (1996). The NCEP/NCAR 40-year reanalysis project. *Bulletin of the American Meteorological Society*, *77*(3), 437–471. https://doi.org/10.1175/1520-0477(1996)077<0437:TNYRP>2.0.CO;2

Kanzow, T., S., Cunningham, W., Johns, J. J., Hirschi, J., Marotzke, M., Baringer, C., et al. (2010). Seasonal variability of the Atlantic meridional overturning circulation at 26.5N. *Journal of Climate*, *23*(21), 5678–5698. https://doi.org/10.1175/2010JCLI3389.1

Large, W., & Yeager, S. (2009). The global climatology of an interannually varying air-sea flux data set. *Climate Dynamics*, *33*(2–3), 341–364. https://doi.org/10.1007/s00382-008-0441-3

Levitus, S., & Boyer, T. P. (1994). *World ocean atlas 1994, NOAA Atlas NESDIS 4: Temperature*. Washington, DC: National Oceanic and Atmospheric Administration.

Levitus, S., Boyer, T., Conkright, M., O'brien, T., Antonov, J., Stephens, C., et al. (1998). *NOAA Atlas NESDIS 18, world ocean database 1998: vol. 1: Introduction* (346 pp.). Washington, DC: US Government Printing Office.

Levitus, S., Burgett, R., & Boyer, T. P. (1994). *World ocean atlas 1994, NOAA Atlas NESDIS 3: Salinity*. Washington, DC: National Oceanic and Atmospheric Administration.

Lozier, M. S., Owens, W. B., & Curry, R. G. (1995). The climatology of the North Atlantic. *Progress in Oceanography*, *36*(1), 1–44. https://doi.org/10.1016/0079-6611(95)00013-5

Lozier, M. S., Bacon, S., Bower, A. S., Cunningham, S. A., de Jong, M. F., de Steur, L., et al. (2016). Overturning in the subpolar North Atlantic program: A new international ocean observing system. *Bulletin of the American Meteorological Society*, *98*, 737–752.

Madec, G. (2008). *Nemo ocean general circulation model reference manual* (Internal report). Paris: LODYC/IPSL.

Mercier, H., P., Lherminier, A., Sarafanov, F., Gaillard, N., Daniault, D., Desbruyères, A., et al. (2015). Variability of the meridional overturning circulation at the Greenland-Portugal OVIDE section from 1993 to 2010. *Progress in Oceanography*, *132*, 250–261. https://doi.org/10.1016/j.pocean.2013.11.001

Mertens, C., Rhein, M., Walter, M., Böning, C. W., Behrens, E., Kieke, D., et al. (2014). Circulation and transports in the Newfoundland basin, western subpolar North Atlantic. *Journal of Geophysical Research: Oceans*, *119*, 7772–7793. https://doi.org/10.1002/2014JC010019

Morgan, P. P., & Pender, L. (2010). *Seawater library version 3.3* (Tech. rep.). Canberra, Australia: CSIRO.

Østerhus, S., Turrell, W. R., Jónsson, S., & Hansen, B. (2005). Measured volume, heat, and salt fluxes from the Atlantic to the Arctic Mediterranean. *Geophysical Research Letters*, *32*, L07603. https://doi.org/10.1029/2004GL022188

Pacanowski, R. (1996). *Mom 2 version 2.0 (beta) documentation users guide and reference model* (Tech. rep., GFDL ocean technical report 3.2, 329 pp.). NOAA-GFDL. Retrieved from https://www.gfdl.noaa.gov/wp-content/uploads/2016/10/manual2.2.pdf

Porter, M., Inall, M., Hopkins, J., Palmer, M., Dale, A., Aleynik, D., et al. (2016). Glider observations of enhanced deep water upwelling at a shelf break canyon: A mechanism for cross-slope carbon and nutrient exchange. *Journal of Geophysical Research: Oceans*, *121*, 7575–7588. https://doi.org/10.1002/2016JC012087

Serreze, M. C., Barrett, A. P., Slater, A. G., Woodgate, R. A., Aagaard, K., Lammers, R. B., et al. (2006). The large-scale freshwater cycle of the arctic. *Journal of Geophysical Research*, *111*, C11010. https://doi.org/10.1029/2005JC003424

Sherwin, T., Aleynik, D., Dumont, E., & Inall, M. (2015). Deep drivers of mesoscale circulation in the central Rockall Trough. *Ocean Science*, *11*(3), 343–359. https://doi.org/10.5194/os-11-343-2015

Smith, D. M., Scaife, A. A., Eade, R., & Knight, J. R. (2014). Seasonal to decadal prediction of the winter North Atlantic oscillation: Emerging capability and future prospects. *Quarterly Journal of the Royal Meteorological Society*, *142*, 611–617. https://doi.org/10.1002/qj.2479

Smith, S. D. (1980). Wind stress and heat flux over the ocean in gale force winds. *Journal of Physical Oceanography*, *10*(5), 709–726. https://doi.org/10.1175/1520-0485(1980)010<0709:WSAHFO>2.0.CO;2

Smith, W., & Wessel, P. (1990). Gridding with continuous curvature splines in tension. *Geophysics*, *55*(3), 293–305. https://doi.org/10.1190/1.1442837

Sverdrup, H. U. (1947). Wind-driven currents in a baroclinic ocean: With application to the equatorial currents of the eastern pacific. *Proceedings of the National Academy of Sciences of the United States of America*, *33*(11), 318–326. https://doi.org/ 10.1073/pnas.33.11.318

UW (2013). *Seaglider quality control manual for basestation 2.08* (Tech. rep.). Seattle, WA: School of Oceanography and Applied Physics Laboratory, University of Washington. Retrieved from http://gliderfs2.coas.oregonstate.edu/sgliderweb/Seaglider_Quality_Control_Manual.html